Facultad de Ciencias

PRUEBAS DE OPERACIÓN DE UN POLARÍMETRO ESPECTRAL PARA DIFERENTES APLICACIONES

(Operating tests of a spectral polarimeter for different applications)

Trabajo de Fin de Máster
para acceder al

MÁSTER EN FÍSICA, INSTRUMENTACIÓN Y MEDIO AMBIENTE

Autor: Andrea Fernández Pérez

Director: José María Saiz Vega
Co-Director: Fernando Moreno Gracia

Julio - 2015

SUMMARY

The simultaneous analysis of the spectrum and state of polarization of light is usually referred to as spectropolarimetry. This technique is widely used for many purposes in fields such as astronomy, medicine, biology or chemistry.

The purpose of this project is to evaluate the possibilities of the imaging dynamic spectropolarimeter for its use over different systems, looking for the necessary adaptions and assessing its performance. On the one hand, we will try to work with the magnification necessary for the examination of microscopic samples, something of great interest for the study of biological systems. Spatial and spectral resolution will be analyzed by obtaining the Mueller matrix of some samples of interest.

On the other hand, we proposed different methods to evaluate, in a fast way, the degree of roughness acquired by metallic surfaces after an industrial process. Several tests will be performed to find the method that provides best results.

KEY WORDS: spectropolarimetry, Stokes vector, Mueller matrix, polarimeter, resolution, applications, metallic surface roughness.

RESUMEN

La espectropolarimetría se basa en el análisis simultáneo de la polarización y el espectro de la luz y es una técnica ampliamente utilizada en diversos campos como astronomía, medicina, biología, química…

El objetivo del proyecto es evaluar las posibilidades de un espectro-polarímetro dinámico de imagen para su aplicación sobre distintos sistemas. Se buscarán las adaptaciones necesarias y se evaluará su comportamiento. Por un lado, se intentará trabajar con el aumento necesario para el examen de muestras microscópicas, algo de gran interés para el estudio de muestras biológicas. Se estudiará la resolución espacial y espectral de algunas muestras representativas a través de la obtención de su matriz de polarización (matriz de Mueller).

Por otro lado, se proponen diferentes métodos para evaluar de forma rápida el grado de rugosidad adquirido por superficies metálicas tras un proceso industrial. Se realizarán varias pruebas de concepto con diferentes montajes experimentales para encontrar el método que proporcione mejores resultados.

PALABRAS CLAVE: espectropolarimetría, vector de Stokes, matriz de Mueller, polarímetro, resolución, aplicaciones, rugosidad de superficies metálicas.

CONTENTS

1 INTRODUCTION

Spectropolarimetry combines the analysis of the spectrum and the polarization state of light. This analysis is of great interest when we study the interaction of light with a system that affects its polarization and, at the same time, shows a spectral dependence. This technique is applied in fields such as astronomy[1], medicine[2], biology[3] or chemistry.

When light interacts with matter it may suffer reflection, refraction, absorption, scattering and dispersion. These processes can affect the state of polarization of the light and have an effect on the polarization of the overall transmittance, reflectance or absorption of the system. Because the interaction may be spectrally selective, polarimetry combines with spectral analysis to produce spectropolarimetry.

1.1 Context and motivation

Polarimetry is used, for example, to study the atmosphere and to find biosignatures[4] in exoplanets. Moreover, it is used to study the radiation and magnetic fields from stars[1], black holes, active galaxies, etc… Other fields where this technique is applied are remote sensing[5], to study fields, tides, or the movement of glaciers; or chemistry, alimentation or quality control, since certain molecules present optical activity.

In the last ten years, polarimetry has found numerous applications in medicine and biology, as part of techniques based on the analysis of light in a noninvasive way, without destroying or modifying the characteristics of the samples.
For instance, it is used to study biological tissues[6,7], where it is very important the imaging characteristic, since the image of the Mueller matrix can provide a lot of information about the structure and composition of the tissue.
It is also used to study cells suspensions[8,9], like cancerous cells mostly, since it can be a helpful tool to detect and diagnose such disease by analyzing properties that make cancerous cells different from regular ones.

The range of application offered by polarimetry is vast, but we will focus on two proposals recently received in the Group of Optics of the Applied Physics Department.

The first one is the study of microscopic samples, and in particular, the analysis of suspensions of cells, sized within the range of 10-20 microns.

The second proposal is the in-situ study of the roughening process of metallic surface inside steel tubes. Though not specifically a polarization problem, the polarization was included as one of the possible approaches.
Here, we are interested in finding a method that allows us to measure the induced surface roughness of steel tubes in a fast and simple way, so that it can implemented in the future as an industrial process.

1.2 Objectives

The aim of this work is to evaluate the capabilities and possibilities of a previously developed dynamic imaging spectro-polarimeter for its use over different systems and samples.

We want to work with samples sized either in the microscopic or in the millimeter scale.
In order to study microscopic sample we need to increase the magnification of the polarimeter and characterize its spatial resolution. Then, one of the goals is to check if we can do imaging spectro-polarimetry in the microscopic scale. In order to do that, we will substitute our former imaging objective by a microscope objective and compare the theoretical and experimental resolution we achieve for two microscope objectives of different magnification. Finally, we want to try the resulting instrument on some small polarization-active and spectrum dependent sample, to complete the process and obtain some Mueller matrix spatially resolved in the microscopic scale.

Regarding the metal surface roughness, we will propose several approaches to the problem and present some initial tests. To do that, we will observe under several experimental configurations, in search of useful parameters connected to the intensity and polarization of the scattered light.

Image recognition or laser profilometry are well-known methods, but not easy to implement for fast-examination.
For an incident coherent beam (laser), light scattered in all directions produces a characteristic speckle pattern. Variation in the average intensity and overall contrast are other classical apporaches[10,11] that have to be tested, but for the deep

roughness of our samples we will try an alternative technique based in the reduction of the spot size in order to work with local reflectance.
The goal of all these approaches is to find the best method and parameter to differentiate the degree of roughness of the surface in an automatic way.

As we want to keep working with both types of samples and in order to not change the experimental setup from one to the other we have set two separate experiments, of which only one uses the main polarimeter.

1.3 Background

The construction and tuning of the main device used in this work, the dynamic imaging spectral polarimeter, has required the work of several people in previous years.

The dynamic polarimeter was developed by Juan Marcos Sanz Casado during his doctoral thesis[12]. After that, the setup was improved firstly by Cristina Extremiana[13] and then by Francesco Carmagnola[14], by implementing, respectively, a discrete wavelength source and an imaging system on a monochromatic basis. After that, the polarimeter was upgraded by implementing a supercontinuum laser source, which alignment and tuning calibration was part of my final degree project[15]. This laser source allows us to select the wavelength at which we want to study the sample, in the visible spectrum (from 480 to 700 nm with a power of at least 1 mW/nm). Now we are able to perform imaging measurements of the Mueller matrix at different wavelengths in the visible spectrum.

Once we have this spectral capability we would like to broaden the type of samples we can study by adding the microscopic feature to the system.

2 THEORY

The main theory that explains how polarimetry works is based in the Mueller-Stokes formalism. This formalism introduces a vector and a matrix to describe, respectively, the polarization state of light and the effect of a system on such state.

But, in order to understand this formalism, we first need to revise some basic concepts about the polarization of light.

2.1 Polarization of light

The polarization is postulated as a transverse property of light. When the electric field **E** of a light beam oscillates in a fully predictable way, we say that the light is polarized.
Light can be polarized in several ways: linear, circular or elliptical in such a way that light beam can be totally polarized, partially polarized or even fully depolarized.

Electric field can be separated into three components in the three directions of space. For a monochromatic polarized beam, of amplitude *A* propagating in the *z* direction with wave number *k* and angular frequency *ω,* the equations of the electric field components are[16]:

$$\begin{gathered} E_x(t) = A_x \cos(\omega t - kz + \varphi_x) \\ E_y(t) = A_y \cos(\omega t - kz + \varphi_y) \\ E_z(t) = 0 \end{gathered} \tag{2.1}$$

In the general case, the projection of the electric field in a plane perpendicular to the direction of propagation is an ellipse, the polarization ellipse (figure 2.1), given by the equation:

$$\frac{E_x^2(t)}{A_x^2} + \frac{E_y^2(t)}{A_y^2} - \frac{2E_x(t)E_y(t)\cos(\varphi)}{A_x A_y} = \sin^2(\varphi) \tag{2.2}$$

Therefore, in the plane $z = 0$:

$$E_x(t) = A_x \cos(\omega t)$$
$$E_y(t) = A_y \cos(\omega t + \varphi) \tag{2.3}$$

Where φ is the phase difference between the two components:

$$\varphi = \varphi_x - \varphi_y \tag{2.4}$$

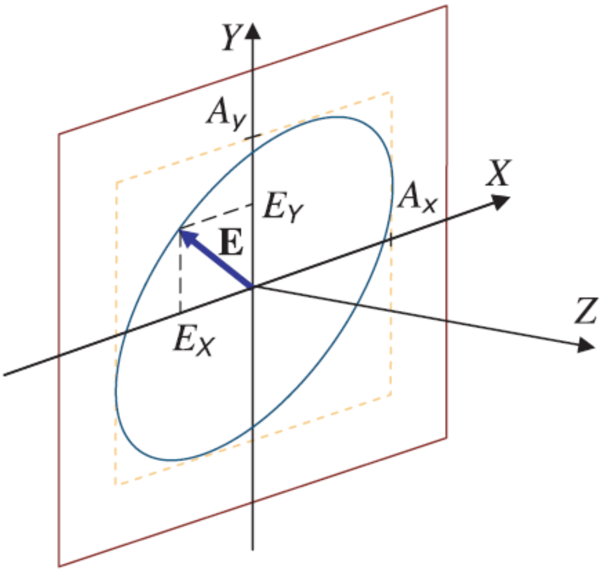

Figure 2.1: polarization ellipse. E_x *and* E_y *are the components of the electric field* ***E****.* A_x *and* A_y *are the amplitudes in* x *and* y *directions. Z is the direction of propagation.*

2.2 Polarimetry

Polarimetry studies the polarization of electromagnetic waves. In order to do that, we need an appropriate formalism to describe the state of polarization of light.

If the light is totally polarized we will use the Jones formalism[17,18] which uses the two components of the electric field **E** to describe the polarization state of light (equation 2.5) and a 2x2 matrix, called the Jones matrix, to describe the action of a non-depolarizing g system over this state.

$$\mathbf{J} = \begin{bmatrix} E_x \\ E_y \end{bmatrix} = \begin{bmatrix} A_x \\ A_y e^{i\varphi} \end{bmatrix} \tag{2.5}$$

Where φ is the phase difference between the two components.

Accordingly, when a light beam with a Jones vector **J** interacts with an optical element the Jones vector at the exit, **J'**, is related to **J** by the Jones matrix **T** of the element.

$$\mathbf{J'} = \mathbf{TJ} = \begin{bmatrix} t_{11} & t_{12} \\ t_{21} & t_{22} \end{bmatrix} \mathbf{J} \tag{2.6}$$

However, if the light is partially polarized this formalism will not be enough so that the Mueller-Stokes formalism is needed[17,18].

2.2.1 Mueller-Stokes formalism

The Mueller-Stokes formalism describes the polarization state of light and the polarization properties of optical elements. Unlike Jones formalism, which is only valid for totally polarized light, Mueller-Stokes formalism provides a mathematical model useful for unpolarized or partially polarized light.

- Stokes vector:

The Stokes vector **S** describes the polarization state of light through four values, called Stokes parameters, defined by G. G. Stokes in 1852.

The Stokes vector can be defined relative to six irradiance measurements *I* performed with ideal polarizers.

$$\mathbf{S} = \begin{bmatrix} s_0 \\ s_1 \\ s_2 \\ s_3 \end{bmatrix} = \begin{bmatrix} I_0 + I_{90} \\ I_0 - I_{90} \\ I_{45} - I_{135} \\ I_R - I_L \end{bmatrix} \tag{2.7}$$

Where I_0 is the result of the measurement performed with an horizontal linear polarizer, I_{90} with a vertical polarizer, $I_{45,135}$ with a 45° and 135° linear polarizer respectively and $I_{R,L}$ with a right handed and a left handed circular polarizer.

The total intensity of light is: $I = I_0 + I_{90} = s_0$.
From this vector, the following polarization parameters are defined: total flux or intensity I, degree of polarization P, degree of linear polarization P_L and degree of circular polarization P_C.

$$I = s_0 \tag{2.8}$$

$$P = \frac{\sqrt{s_1^2 + s_2^2 + s_3^2}}{s_0} \tag{2.9}$$

$$P_L = \frac{\sqrt{s_1^2 + s_2^2}}{s_0} \tag{2.10}$$

$$P_C = \frac{s_3}{s_0} \tag{2.11}$$

A totally polarized beam has $P = 1$ and a partially polarized beam has $P < 1$.

Another way of writing the Stokes vector is:

$$\mathbf{S} = \begin{bmatrix} s_0 \\ s_1 \\ s_2 \\ s_3 \end{bmatrix} = \begin{bmatrix} E_x E_x^* + E_y E_y^* \\ E_x E_x^* - E_y E_y^* \\ E_x E_y^* + E_y E_x^* \\ i\left(E_x E_y^* + E_y E_x^*\right) \end{bmatrix} = \begin{bmatrix} A_x^2 + A_y^2 \\ A_x^2 - A_y^2 \\ 2A_x A_y \cos\varphi \\ 2A_x A_y \sin\varphi \end{bmatrix} \tag{2.12}$$

The Stokes vector for a partially polarized beam can be represented as a superposition of a completely polarized Stokes vector $\mathbf{S_P}$ and a completely unpolarized Stokes vector $\mathbf{S_U}$.

$$\mathbf{S} = \begin{bmatrix} s_0 \\ s_1 \\ s_2 \\ s_3 \end{bmatrix} = \mathbf{S_P} + \mathbf{S_U} = s_0 P \begin{bmatrix} 1 \\ s_1 / P s_0 \\ s_2 / P s_0 \\ s_3 / P s_0 \end{bmatrix} + \left(1 - P\right) s_0 \begin{bmatrix} 1 \\ 0 \\ 0 \\ 0 \end{bmatrix} \tag{2.13}$$

- Mueller matrix

The Mueller matrix **M** is a 4x4 matrix with real elements that represents the effect of an optical device over the polarization state of the light. It was developed in 1943 by Hans Mueller. This matrix transforms an incident Stokes vector **S** into the exiting Stokes vector **S'**.

$$\mathbf{S'} = \begin{bmatrix} s'_0 \\ s'_1 \\ s'_2 \\ s'_3 \end{bmatrix} = \mathbf{MS} = \begin{bmatrix} m_{00} & m_{01} & m_{02} & m_{03} \\ m_{10} & m_{11} & m_{12} & m_{13} \\ m_{20} & m_{21} & m_{22} & m_{23} \\ m_{30} & m_{31} & m_{32} & m_{33} \end{bmatrix} \begin{bmatrix} s_0 \\ s_1 \\ s_2 \\ s_3 \end{bmatrix} \tag{2.14}$$

The Mueller matrix fully characterizes a medium for a given wavelength and a geometrical configuration because it contains within its elements all of the polarization properties.

The difficulty of a Mueller matrix analysis is double: first we need to obtain a reliable matrix, and then we have to analyze it in a proper way. For example the Mueller matrix can be decomposed in several matrices, each of one representing independent physical actions of the system (diattenuation, retardation and depolarization), thought this process is out of the scope of this work.

Any Mueller matrix can be written in the form[19]:

$$\mathbf{M} = m_{00} \begin{bmatrix} 1 & \mathbf{D^T} \\ \mathbf{P} & \mathbf{m} \end{bmatrix} \tag{2.15}$$

Where $\mathbf{D^T}$ is the transposed diattenuation vector, **P** is the polarizance vector and **m** is a 3x3 matrix related with the optical activity of the medium.

Finally, if the light beam passes through several optical elements the resulting Mueller matrix $\mathbf{M_T}$ is the product of the matrices of each element in reverse order, this being one of the main advantages of the formalism:

$$\mathbf{M_T} = \mathbf{M_n M_{n\text{-}1} \ldots M_2 M_1} \tag{2.16}$$

2.2.2 Mueller matrix examples

As I already explained, the Stokes vector characterizes the polarization state of a light beam. Table 2.1 shows some examples of Stokes vectors.

Polarization state	*Unpolarized*	*Horizontal/Vertical linear*	*±45° linear*	*Dextro/Levo circular*
Stokes Vector	$\begin{bmatrix}1\\0\\0\\0\end{bmatrix}$	$\begin{bmatrix}1\\\pm1\\0\\0\end{bmatrix}$	$\begin{bmatrix}1\\0\\\pm1\\0\end{bmatrix}$	$\begin{bmatrix}1\\0\\0\\\pm1\end{bmatrix}$

Table 2.1: Stokes vector for some basic polarization states.

Optical element	*Vacuum*	*Horizontal/Vertical linear polarizer*	*±45° linear polarizer*
Mueller matrix	$\begin{bmatrix}1&0&0&0\\0&1&0&0\\0&0&1&0\\0&0&0&1\end{bmatrix}$	$\begin{bmatrix}1&\pm1&0&0\\\pm1&1&0&0\\0&0&0&0\\0&0&0&0\end{bmatrix}$	$\begin{bmatrix}1&0&\pm1&0\\0&0&0&0\\\pm1&0&1&0\\0&0&0&0\end{bmatrix}$

Optical element	*Absorbent medium*	*Linear polarizer (a)*	*Linear retarder (0°, δ)*
Mueller matrix	$\begin{bmatrix}a&0&0&0\\0&a&0&0\\0&0&a&0\\0&0&0&a\end{bmatrix}$	$\begin{bmatrix}1&c_{2\alpha}&s_{2\alpha}&0\\c_{2\alpha}&c_{2\alpha}^2&s_{2\alpha}c_{2\alpha}&0\\s_{2\alpha}&s_{2\alpha}c_{2\alpha}&s_{2\alpha}^2&0\\0&0&0&0\end{bmatrix}$	$\begin{bmatrix}1&0&0&0\\0&1&0&0\\0&0&c_\delta&s_\delta\\0&0&-s_\delta&c_\delta\end{bmatrix}$

Optical element	*Ideal depolarizer*	*Partial depolarizer*	*Linear retarder (φ, δ)*
Mueller matrix	$\begin{bmatrix}1&0&0&0\\0&0&0&0\\0&0&0&0\\0&0&0&0\end{bmatrix}$	$\begin{bmatrix}1&0&0&0\\0&d_1&0&0\\0&0&d_2&0\\0&0&0&d_3\end{bmatrix}$	$\begin{bmatrix}1&0&0&0\\0&c_{2\varphi}^2+c_\delta s_{2\varphi}^2&(1-c_\delta)s_{2\varphi}c_{2\varphi}&-s_\delta s_{2\varphi}\\0&(1-c_\delta)s_{2\varphi}c_{2\varphi}&s_{2\varphi}^2+c_\delta c_{2\varphi}^2&s_\delta c_{2\varphi}\\0&s_\delta s_{2\varphi}&-s_\delta c_{2\varphi}&c_\delta\end{bmatrix}$

Table 2.2: Mueller matrix for some optical elements[12] *where a is the azimuth of the polarizer, δ is the phase introduced by the retarder, φ is the azimuth with respect to the incident beam, a is the absorbance,* c_x *= cos (x) and* s_x *= sin(x) (x is 2φ or δ).*

The optical properties of a sample determine the elements values of its Mueller matrix elements.
Moreover, the values can change along the spectrum since the optical behavior of the sample may depend on the wavelength.

Table 2.2 shows the Mueller matrix of some basic optical elements as linear polarizers or retarders. The Mueller matrix of a sample can often be described as a combination of these, depending on whether the sample polarize the light, present absorption, introduce a phase, etc…

2.3 Surface roughness

Surface roughness is a measure of the topographic relief of a surface[20]. It can be defined as the finish of a surface, determined by all its irregularities and shown, for instance, in the smoothness or steepness of its profile. The measurement of the surface roughness is very important since, for example, it can determine the quality, resistance or future performance of the material that is limiting.

The surface roughness can be expressed through several amplitude parameters, being the most used the roughness average R_a which is the mean value of the deviations from the mean line in a measured length L. This is, the mean value of the distances from peaks or valleys to the mean line of the surface. The value R_a is given by equation (2.17):

$$R_a = \frac{1}{L}\int_0^L \left| f(x) \right| dx \tag{2.17}$$

Where $f(x)$ is the function that describes the profile of the surface.

Surface height variations Δy can be also measured from a mean surface level and expressed through the root mean square (*rms*) or *rms* roughness value:

$$rms = \sqrt{\frac{1}{N}\sum_{i=1}^{N}\left(y_i - <y>\right)^2} \tag{2.18}$$

Where y_i is the value of the surface profile at point i and $<y>$ is the mean surface value.

Although the *rms* value does not characterize completely the roughness, since various surface profiles can have the same *rms*, it is useful in the way that it provides the height variations or depth of the roughness.
Another parameter to characterize the roughness is the surface spatial wavelengths or correlation length that is the separation between similar surface features along the surface.

Currently, there exists several methods to measure the roughness of a surface, and basically, they can be classified in two main blocks: contact method and non-contact methods.

Contacts methods are based on the measurement of the surface profile by means of a stylus perpendicular to the surface along a straight line. The problem of this method is that it can damage fragile surface and they are only valid for solid materials. In addition, they are slow and offer single-line observation. On the contrary, non-contact method allow to measure the roughness without touching the surface and often covering a wide field of the sample. They are based on interferometry or in measurements of the scattered light properties, by illuminating the sample with a laser and measuring the scattered light at a certain angle that might include backreflectance.

For instance, a method to measure the surface roughness, based on the measurement of the scattered light, is the Total Integrated Scattering (TIS) [20]. This method consists on collecting and measuring the scattered light and the specularly reflected light. The TIS parameter relates to the surface roughness by means of the equation (2.19):

$$TIS = \frac{V_{sample,scattered}}{V_{sample,\mathrm{specular+scattered}}} \cong \left(\frac{4\pi\delta}{\lambda}\right)^2 \tag{2.19}$$

Where *V* is voltage, δ is the *rms* roughness and λ is the wavelength.

Others methods based on scattering measurement are Angle-Resolved Scattering (ARS) that analyze the angular distribution of the light scattered by the sample, or the Bidirectional Reflectance Distribution Function (BRDF), defined as the scattered surface radiance divided by the incident surface irradiance. However, all this method are usually used for small *rms* roughness values.

Surface roughness measurement can be done using electron microscopes, too, which allow to measure surface features too small to see with optical microscopes.

Finally, other methods to measure surface roughness use comparison with reference samples or the touch or eyesight to differentiate the roughness but they provide very subjective results.

3 EXPERIMENTAL SETUP

This section will describe the experimental setup used to study the different samples and to perform the measurements. We present it in two parts: first the imaging dual rotating polarimeter adapted to the microscopic domain, and secondly, the setups used to perform tests on rough surfaces.

3.1 Imaging Dual Rotating Compensator Polarimeter

The main instrument used is the Dynamic Rotating Compensator Polarimeter (DRCP) (figure 3.1) developed by Juan Marcos Sanz Casado and located in the Optics laboratory at the Universidad de Cantabria. The device has been recently upgraded by Francesco Carmagnola who added a CCD detector and wrote software in OCTAVE code to obtain a fully Mueller imaging system.

Last year, a supercontinuum laser was added as the light source, so that now we can perform measurements of the Mueller matrix at different wavelengths.

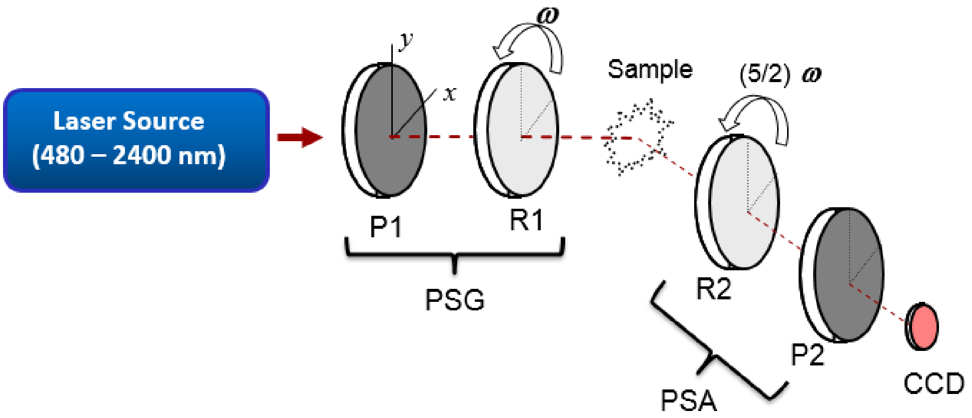

Figure 3.1: Dual Rotating Compensator Polarimeter[12].

The polarimeter consists of a supercontinuum laser source; a polarization state generator (PSG) composed of a polarizer and a rotating quarter-wave plate; a polarization state analyzer (PSA) composed of an analyzer and a rotating quarter-wave plate; and a detector. By replacing the detector by a CCD and a camera objective we are able to obtain a full image of the illuminated area of the sample, and a full matrix for each point of such image.

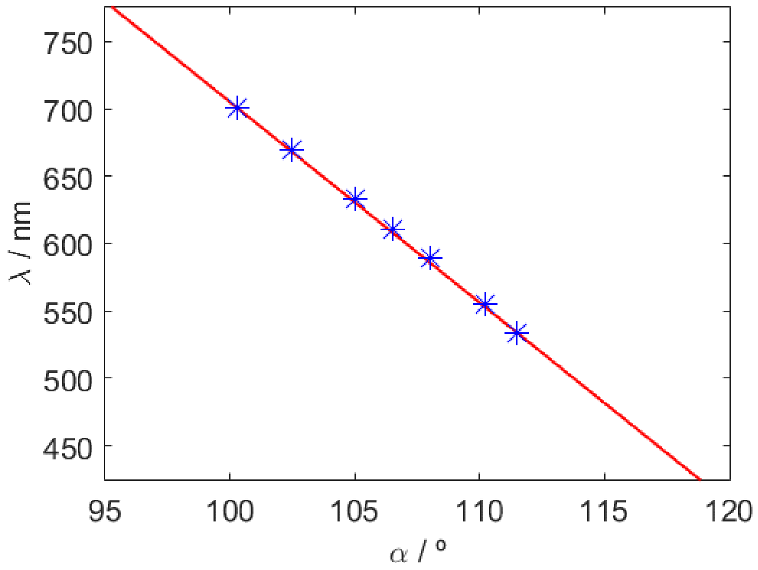

Figure 3.2: wavelength selection after the calibration of the rotatory stage.

The laser source provide a continuous spectrum in the visible region. The wavelength can be selected in a range from 480 nm to 700 nm by means of a diffraction grating placed on a rotatory stage, and a pinhole. Figure 3.2 shows the wavelength selected as a function of the position of the stage, in degrees.

Right after the laser source a long focal-length lens is placed in order to control the spot size and to focus light on the sample. Between the PSG and the PSA there is a sample holder where the sample we want to study is placed. The intersection point formed by the alignment axis system and the detection system axis corresponds to the center of the observed area of the sample.
According to the dynamic measurement technique, both quarter-wave plates rotate synchronously with a speed ratio of 5:2 so we can complete a full Fourier cycle sampled with 200 measurements of the intensity. The data obtained from the cycle is saved in raw format and it is used to calculate, by means of a Fourier analysis[21], the Mueller matrix (MM) of the sample placed between the PSG and the PSA.

The PSA together with the detector are set in an arm which can rotate so that the MM of a sample can be measured in different configurations such as transmission, reflectance or scattering. This movement is performed by a motor controlled with software. The two wave plates both are moved by stepper motors and when the full cycle is finished they return to its original position.

3.1.1 Boot protocol and calibration

When we want to perform a measurement of the Mueller matrix it is very important to follow a boot protocol to guarantee the correct work of the experimental set up.

Moreover, we need to calibrate the polarimeter every time we modify an optical element. The calibration of the polarimeter is a very important point of the work as it is essential for a good performance of the system.
The calibration involves expanding the beam of the laser and doing a full cycle of measures without placing a sample between the PSA and the PSG.

After turning on the full experimental setup it is time to calibrate the system.
With both arms of the polarimeter aligned, we should start with the PSA, this is, the farthest elements, as seen from the source.
With the lights off we should cover the camera with a white foil in order to avoid CCD sensor's damage. Next, we should remove both wave plates and search for the maximum contrast with the laser. After this, we cross the analyzer (PSA) and we look for the minimum intensity.

The next step is to place the PSA wave plate and, as we just did with the polarizer, we look for the minimum, by rotating it until the neutral axis of the wave plate is aligned with the PSA polarizer. At this point we should not forget to turn on the wave plate motor. We repeat the process for the PSG wave plate.
We move on now to the PSA polarizer and, the one away from the laser and we rotate this polarizer 90º clockwise and 22.5º counterclockwise. This 22.5º is not a random angle but it is known to be an adequate value to minimize the error in the measured cycle.
After this procedure, we are ready to do a measurement cycle. As there is no sample, we measure the intensity transmitted by the air. The Mueller matrix of the air, $\mathbf{M}_a$, is approximated by the vacuum Mueller matrix $\mathbf{M}_v$: the 4x4 unit matrix.

The calibration process provides the necessary values of the variables that characterize the polarimeter: the phase introduced by the retarders and their transmittance and azimuths of retarders and polarizers.

3.1.2 Addition of a microscope objective

As I already commented in the introduction, we are interested in micron-sized samples, ranging from a few microns to some tenths.

We need to produce a good magnification and characterize the spatial resolution of the polarimeter. This is the reason why we have added a microscope objective, placed between the sample holder and the PSA (figure 3.4).

We have used two different infinity corrected microscope objectives (Figure 3.3) with a 5x and 10x magnification, each one with a numerical aperture $NA = 0.13$ and $NA = 0.30$ respectively.

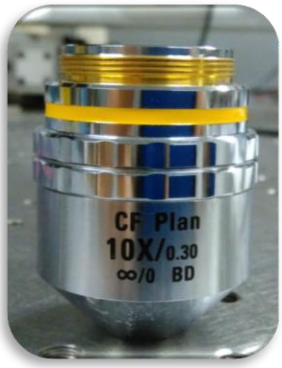

Figure 3.3: microscope objective with a 10x magnification.

The image of the sample is focused onto the CCD of the camera (its ordinary objective was removed). Longitudinally adjusting the microscope objective we obtained a sharp image of the object (as in the intermediate image of a common microscope).

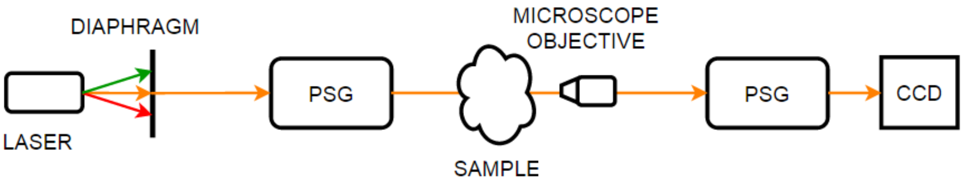

Figure 3.4: diagram of the polarimeter after the addition of the microscope objective.

3.2 Surface roughness setups

In order to perform some initial probes on the rough surfaces, we have designed several setups in which scattered light coming from surfaces of different roughness is observed.

3.2.1 Intensity measurement

This setup corresponds to the simplest possible configuration (figure 3.5): the surface is illuminated by a given beam and the scattered intensity for a given direction is observed for different surfaces.

The source was a He-Ne laser source ($\lambda = 633$ nm) which emits linear polarized light perpendicular to the table (This property of the source allowed us to study the possible polarization dependence).
The sample is placed on a stage that allows us to change the height and the position in the y axis. This allows us to measure the intensity at different positions of the sample, since it has a curve surface. The scattered light is focused onto a detector by a collecting lens. The angle of measurement θ can also be changed.

Initially, the signal-to-noise ratio was very low so we had to add a chopper with a lock-in amplifier to the setup so that the signal was amplified (the chopper rotates with a frequency $\nu = 1500$ r.p.m). Finally we sent the signal to an oscilloscope.

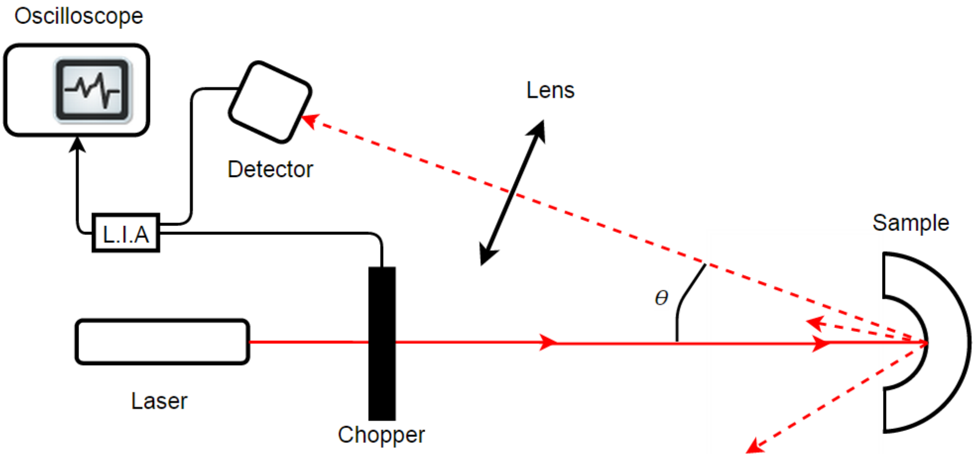

Figure 3.5: experimental setup to measure the intensity of scattered light by the sample at several angles θ.

3.2.2 Reflectance of focused beams

As before, the sample is illuminated with a laser beam of $\lambda = 633$ nm. We focus the beam on the sample by means of a 4f systems, with two convex lenses of focal $f_1 \approx 80$ mm and $f_2 = 150$ mm (figure 3.6), the first one to focus and expand the beam from that point and the second to focus on the sample. The second lens must have a high numerical aperture since we want to collect as large scattered angle as possible. Between the two lenses we placed a beam splitter so that the scattered light can be redirected to the camera. If focused, the camera would monitor the light spot on the surface, but if it is out of focus it may image the spatial distribution of the light cone that is producing that particular image. In other words: we propose to analyze the "local specular" effect of the surface, since our spot is smaller than the roughness length of the surface (see figure 3.7). Finally we connect the camera to a computer to see the images.

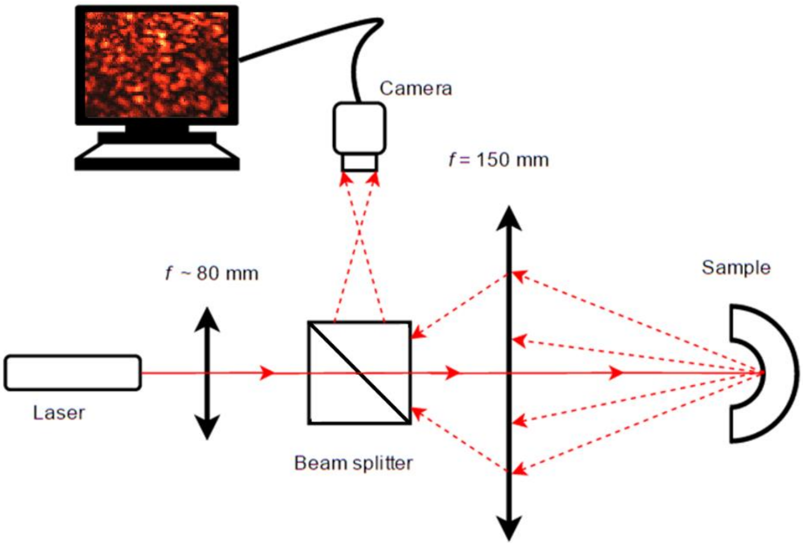

Figure 3.6: initial experimental setup to measure the local specular of the surfaces.

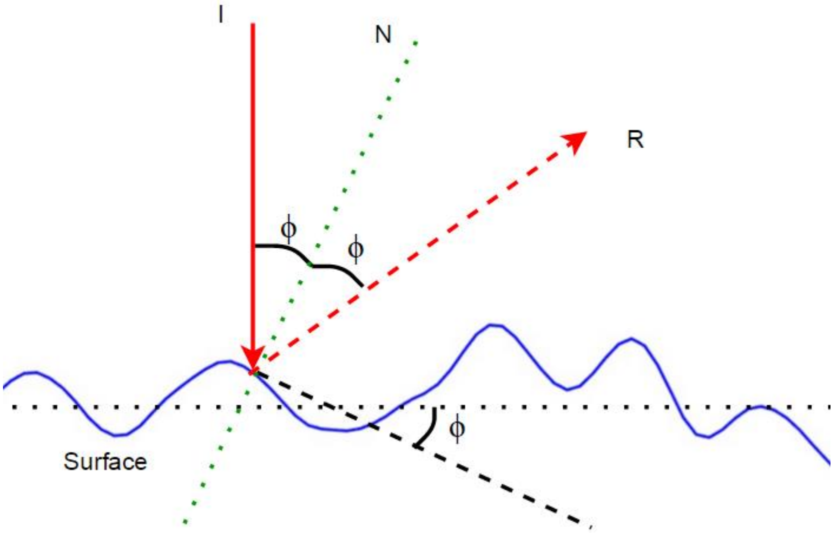

Figure 3.7: scattering of the focused beam. I is the incident beam, N represents local the normal to the surface and R is the direction where the strongest scattering is expected.

When the surface's slopes are large, so are the fluctuation amplitudes and this has forced us to make an important modification in the setup (see figure 3.8). We have added a screen of 25x13 cm and, by moving the sample along the *z* axis (height), we take several pictures of the screen.
The distance between the screen and the point of impact in the sample is 19 cm so we have an angular field of around 19º.

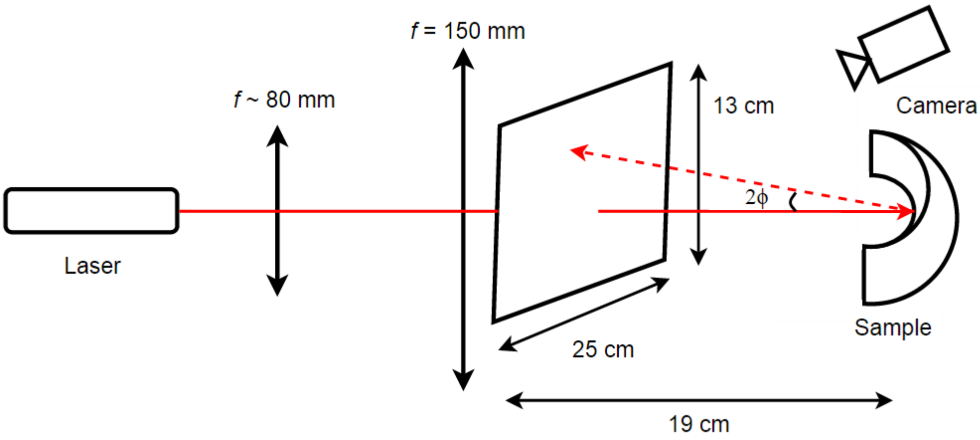

Figure 3.8: experimental setup to measure the angular distribution of the local reflection.

3.2.3 Speckle measurement

Starting from the configuration described in figure 3.6, and since we are using a coherent source, the camera can be used to collect the speckle intensity and then measure the speckle contrast that, in turn, is related to the surface roughness, though only for small values of the *rms*, which is not our case, most likely.

4 SAMPLES AND RESULTS I: MICROSCOPIC POLARIMETRY TESTING

In this section we present the results related to polarimetry. First of all, we describe the samples we have used to check the spatial resolution and study the spectral sensitivity of the system.

Next, we present the main results obtained in this part, related to the imaging capabilities after implementing the microscope objectives and the calculation of Mueller matrices at several wavelengths, from experimental measurements.

4.1 USAF 1951 Test Target

The USAF 1951 Test (figure 4.1, left) is based on a pattern of parallel lines (figure 4.1, right) 2.5/*x* mm long and 0.5/*x* mm wide separated by spaces of 0.5/*x* mm wide where *x* is the number of line pairs/mm. Each line is five times longer than wide.

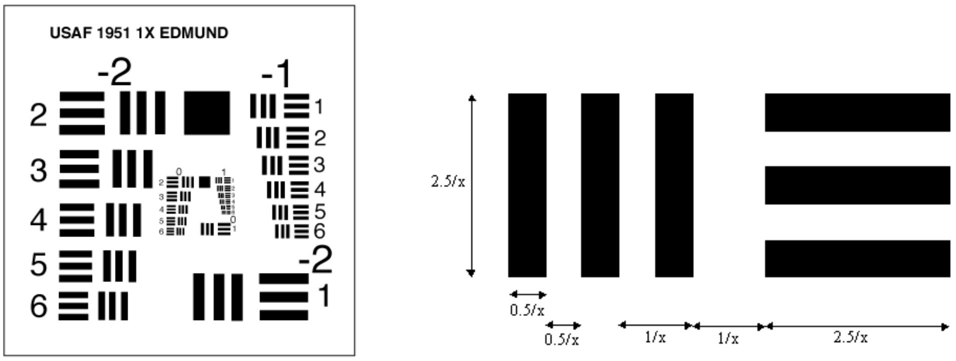

Figure 4.1: USAF 1951 Test Chart (left) and structure of one element of the chart (Left image from http://www.efg2.com/Lab/ImageProcessing/TestTargets).

It is used in order to evaluate the resolving power of an optical system. For instance, it provides with the spatial frequencies to evaluate the MTF (modulation transfer function) of instruments.

The target has several groups of six elements. Each element is formed by two sets of lines: 3 vertical and 3 horizontal and is identified with a group number from -2 to 7 and an element number from 1 to 6.

The size of each target element within a group is progressively smaller by a factor $2^{-1/6}$ and the resolution x increases by the factor $2^{1/6}$. At the same time, the resolution duplicates from group to group.

Moreover, the target can be positive, with black lines separated by white spaces; or negative, with white lines separated by dark spaces (in our case both of them lead to similar results).

Each pair of a white line (or space) and a black line is known as a cycle so with this Test Chart we can know the resolution of the setup in cycles/mm or line pairs per millimeter (lp/mm).

The resolution is given by the equation 4.1:

$$Resolution\left[lp/mm\right] = 2^{\left(GroupNumber + \frac{ElementNumber - 1}{6}\right)} \tag{4.1}$$

When the period between the lines decreases, so does the contrast, until we are not able anymore to differentiate the number of black or white lines. This point indicates the resolution limit of the system. This way, if we take an image of the target, the resolution of our system will be given by the group and element numbers of the black and white bars just before they begin to blur together.

A test target of this kind, with groups numbers from 0 to 7, will be used in this work in order to analyze the resolution of the images taken.

4.2 LCD-TFT Screen

An LCD-TFT screen is a display surface that uses the properties of liquid crystal to show images. Liquid crystal is a material with light modulating properties. When an electric field is applied to the crystal the molecules change the orientation and are able to change the polarization of light incident on it.

An LCD screen is formed by several films of different materials which includes polarizers, diffuser materials and a liquid crystal. Specifically, we present here the structure of an LCD screen form a digital camera (Figure 4.2 left). The inner layer is a reflective surface (9) to send the light to the viewer, followed by a light guide plate (8) and a thin film that distributes the light uniformly all over the surface (7). The next layers (5 and 6) are some diffuser and "prism films" designed to bend the beams, which provide a better illumination of the screen and better contrast. Following, we get to the central sandwich of the screen. In the front and in the back, there are two linear polarizers (1 and 4) in crossed position. In the center there is a glass piece in which is the liquid crystal (3). On the top of the glass sheet and before the front polarizer, there is a color filter layer (2), divided into cells of the three main colors (blue, red and green).

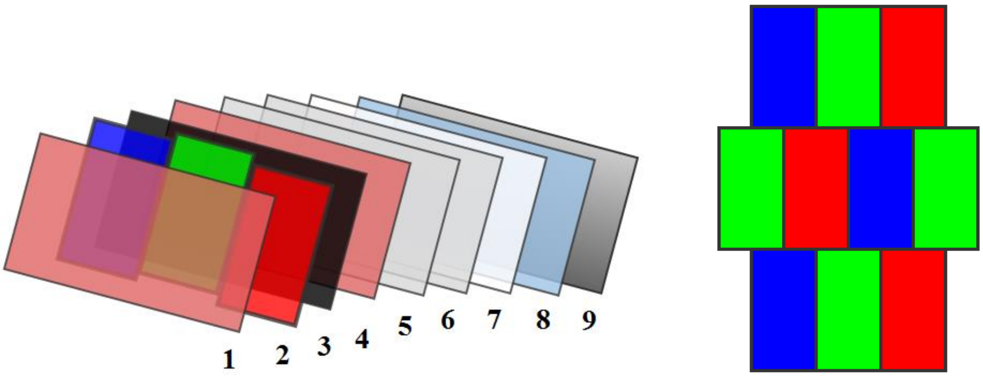

Figure 4.2: layered structure of a LCD-TFT screen (left) and color filters structure (right).

In particular we are interested in the layer with the color filters so that, on one hand, we can make use of the new resolution capability and see the three different color filters and, on the other hand, we could observe the behavior at different wavelengths which is expected to be different since we have filters of three different colors.

We have removed all the extra layers so that we only remain with the central sandwich that contains the liquid crystal and the color filters (layers 2 and 3). The color filters have a structure shown in figure 4.2 right. Each cell has a dimension of 150 x 70 microns approximately.

4.3 Spatial resolution

We have studied the spatial resolution achieved with a microscope objective for two different nominal magnifications. We compared also the limit resolution given by the numerical aperture of the objectives and the experimental values obtained from the USAF target.

Before placing the microscope objective we were imaging a sample region of approximately 1 cm^2 (actually a circular region with a radio of 0.5 cm) in a section of 640x640 pixels of the CCD.

For the tests with the microscope objectives, we have used the full area of the CCD (1392x1040 pixels) and in order to know the resolution, we have imaged the USAF 1951 target. The measurements were taken at $\lambda = 616$ nm. Figure 4.3 shows the image of this target when we use the 5x objective. The red frame indicates the part imaged with the 10x objective, shown in figure 4.4.

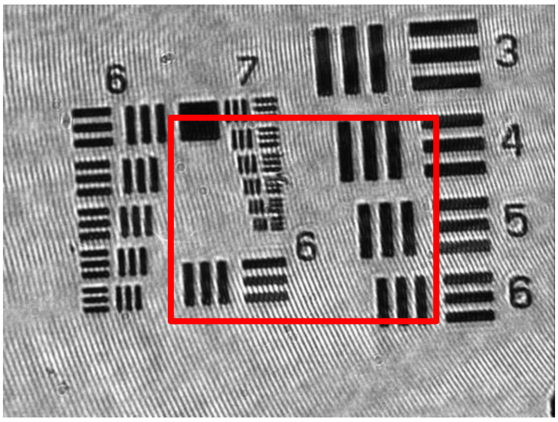

Figure 4.3: image of the USAF 1951 test target with the 5x microscope objective.

The red frame in the figure 4.4 left corresponds to the smallest element (group 7 and element 6) of the target. The lines of this element have a length of 10.96 μm, being the space between them of 2.19 μm.

The theoretical resolution is related to the minimum distance at which two points are observed separate, *r*, and this is given by the numerical aperture, *NA*, of the microscope objectives[22]:

$$r = \frac{0.61\lambda}{NA} \tag{4.2}$$

Figure 4.5 shows the theoretical resolving distance as a function of the wavelength for both objectives. The dots show the experimental resolving distance achieved with the target at $\lambda = 616$ nm.

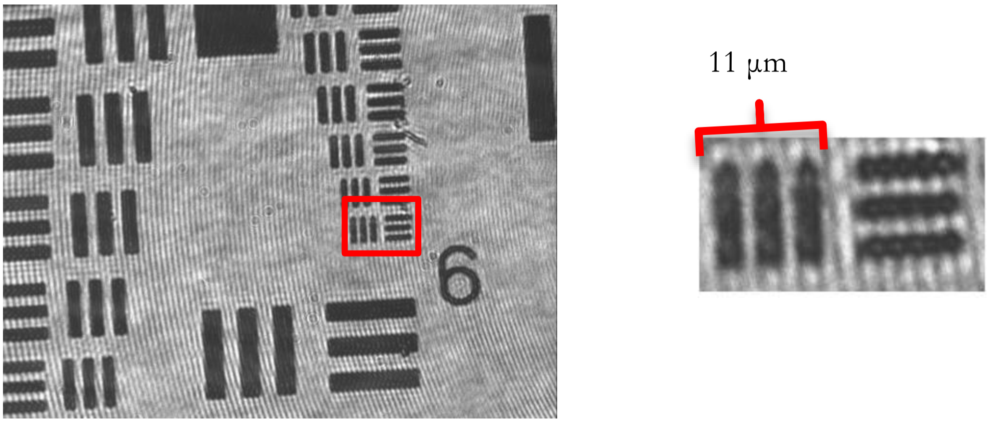

Figure 4.4: image of the USAF 1951 test target with the 10x microscope objective (left) and section in the red frame (right).

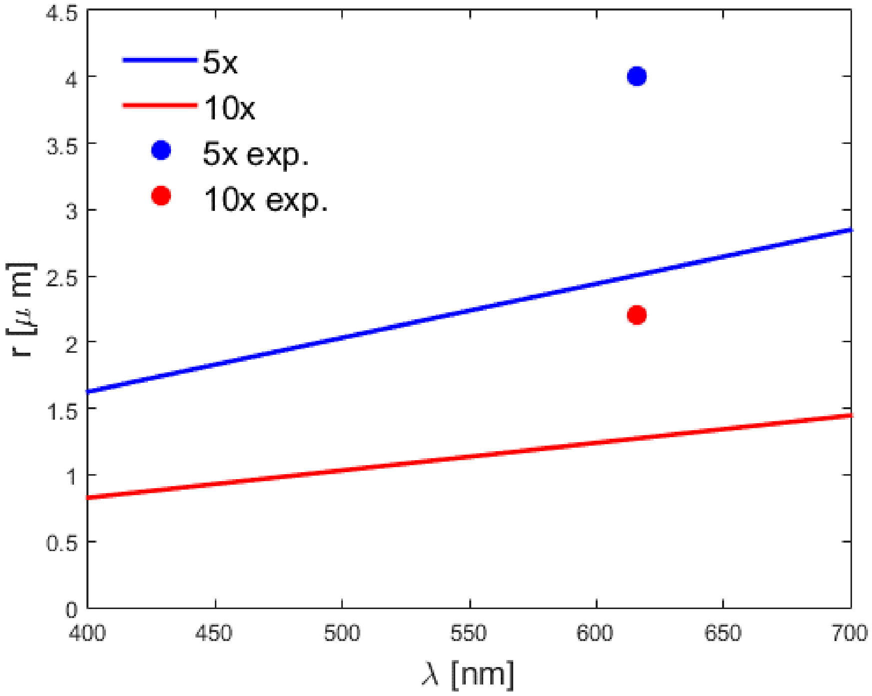

Figure 4.5: minimum resolved distance, r, as a function of the wavelength. Points represent the experimental limit, or verified points.

The experimental resolution is given by the measurements of the USAF target. As we can see in figures 4.3 the smallest elements is barely resolved. However, with the 10x objective we perfectly resolve the smallest element of the target. As we know the length and width of each element in the target, this means that experimental resolution is around 3 or 4 µm for the 5x objective and is smaller than 2.2 µm in the case of the 10x objective for the measured wavelength. With this verified values, the experimental resolution is consistent with the theoretical prediction for each objective.

We have calculated the actual experimental magnification of the objective, since they are not working on the configuration they are supposed to.
Table 4.1 offers a summary of the resolution, magnification and the scale.

Microscope Objective	***5x***	***10x***
Scale [pix./µm]	2.78	5.74
Experimental resolved distance r (experimental resolution)	~3-4 µm (~143 lp/mm)	< 2.2 µm (> 228 lp/mm)
Theoretical magnification	5	10
Experimental magnification	12.90	26.72

Table 4.1: resolving distance and magnification achieved with the two microscope objectives.

4.4 Spectral resolution

In figures 4.3 and 4.4 it can be clearly observed that an interference pattern appears, probably due to multiple reflections in the layer protecting the CCD. It can be ignored if we are imaging very large objects but it is important if we want to see small details.

Given its interferencial nature, this problem can be solved by averaging several images in a range of wavelengths. This will cause a loss in spectral resolution for the benefit of the spatial one.

Figure 4.6 shows the comparison between an image taken at $\lambda = 616$ nm and the average image in intensity of 21 images in a range from 616 to 601 nm.
As we can see the interference pattern is reduced and the lines are better resolved, especially the vertical ones.

With the rotating stage we are able to fix a wavelength in the visible spectrum with a precision of 2 nm approximately. Now, as a result of the average in order to reduce the interference pattern, we reduce the spectral resolution down to 15 nm.
So, if we can perform a measure at a central wavelength λ_0 we will have to cover a range of approximately 15 nm:

$$\Delta\lambda = (\lambda_0 \pm 8\text{ nm})$$

This reduces the spectral resolution but this may be not necessary if we are working with larger samples. However, if we want to see details, it is useful to eliminate this pattern.

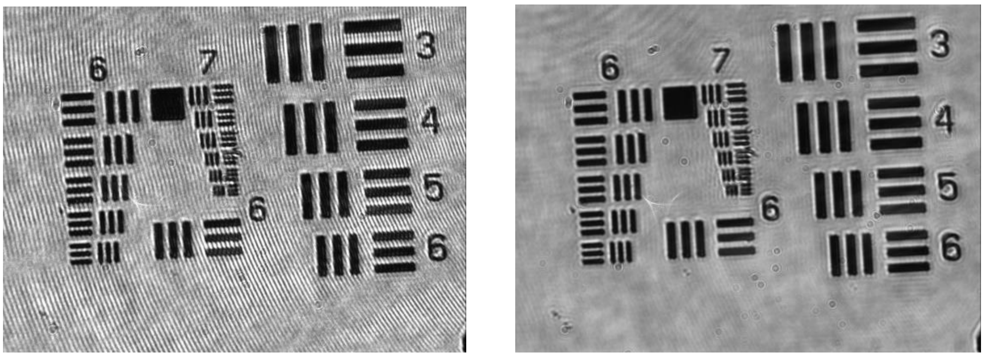

Figure 4.6: comparison between a single image of the USAF target at 616 nm and the average of 21 images from 616 to 601 nm.

4.5 Spectral analysis: LCD

In order to explore the capability of the polarimeter to measure at several wavelengths and to perform measurement of small samples we have chosen as a test sample the LCD screen depicted in section 4.1.2. We have imaged the set of two layers: the color filters and the liquid crystal. Each color cell is sized 150 x 70 microns approximately, and our field of view includes several of them.

We have performed measurements of the Mueller matrix at 4 different wavelengths and with the 5x microscope objective, which is enough for the purpose.

Figure 4.7 shows the Mueller matrix for the wavelengths listed in table 4.5 where we can see that the three different filters are resolved.
Element m_{00} indicates the transmission, this is the measured intensity. In this element we can see that the different color cells light up more or less depending on the wavelength.

Elements in column and row one are close to zero, indicating that both the polarizance and diattenuation are practically nonexistent. The elements in the left 3x3 matrix show the activity of the sample.

The effect of the liquid crystal and the color filter may be a combination of a lineal retarder whose optical axis is rotated a certain angle and a rotation. The values of the phase and rotations, which seems to slightly vary with the wavelength, could be obtained by means of a polar decomposition, but this is out of the scope of this work.

Lambda [nm]	Color
633	Red
586	Yellowish orange
556	Yellowish green
526	Dark green

Table 4.2: experimental wavelengths used to perform the measurements of the Mueller matrix.

$\lambda = 633$ nm

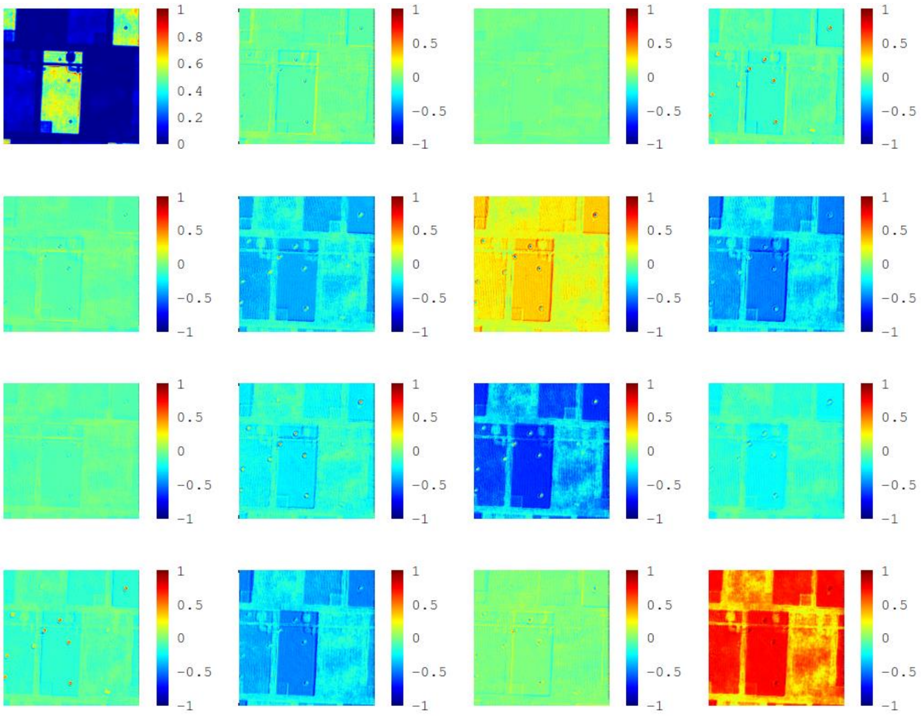

λ = 586 nm

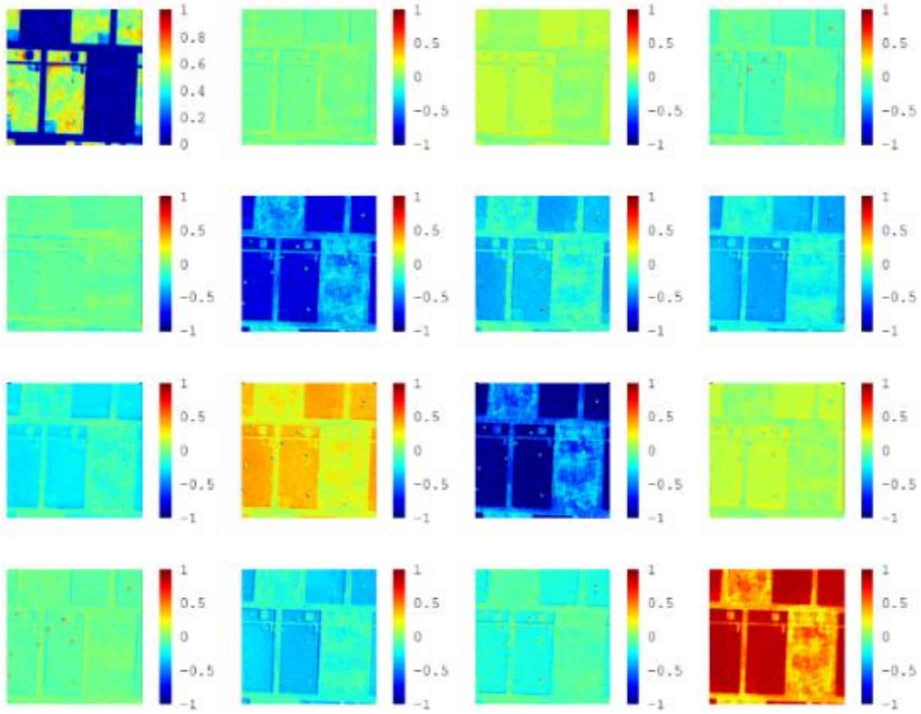

λ = 556 nm

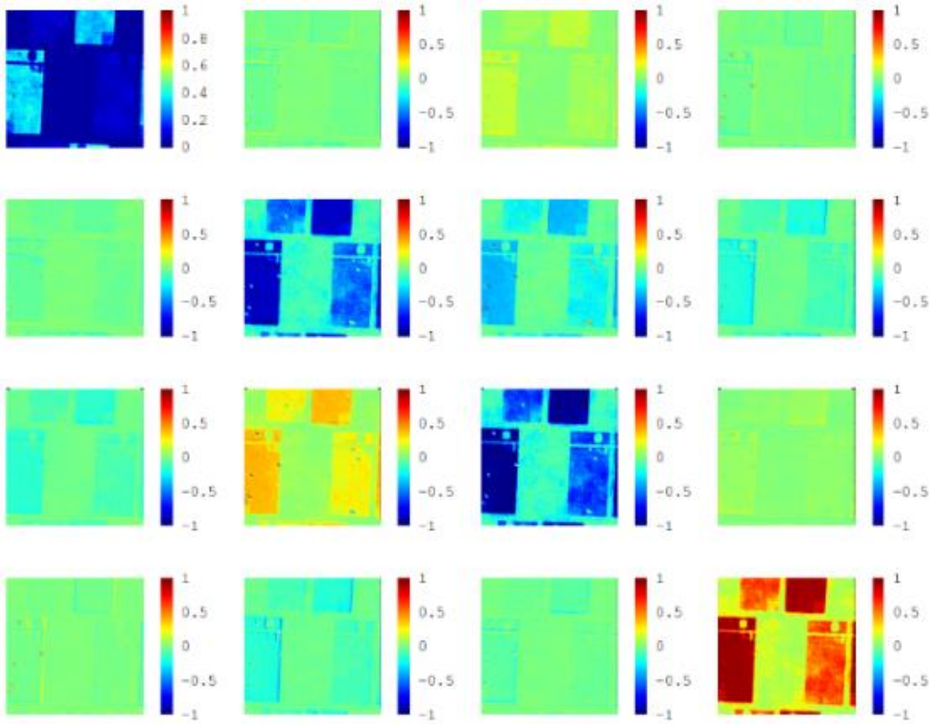

$\lambda = 526$ nm

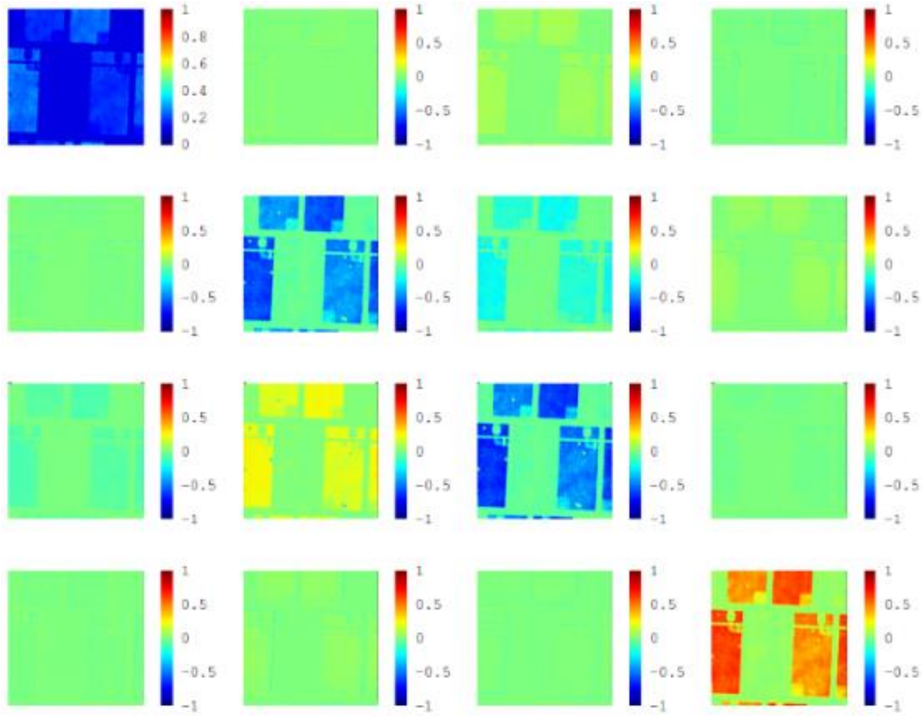

Figure 4.7: Mueller matrices images (640x640 pix.) at four wavelengths (table 4.5) of the color filters and liquid crystal in a LCD screen.

5 SAMPLES AND RESULTS II: SURFACE ROUGHNESS

In this section we present the results related to the study of metallic surface roughness. We describe the samples and show the main results obtained with each of the methods proposed.

5.1 Samples

The samples we are working with are steel tubes of which the surface of interest is the inner one (see figure 5.1). Inner and outer radius are $r_i = 2$ cm and $r_o = 2.5$ cm. The inner surface has received a strengthening process that produces a corrugation. We have samples which have suffered an increasingly severe process, including one that has not been process at all. We are interested in knowing the roughness of such surface in search of a way of characterizing the quality of the strengthening operation done on the processed tubes.

In a future, an optical test could be included in an industrial process. Therefore, we need a simple method which allow measurement in real time.

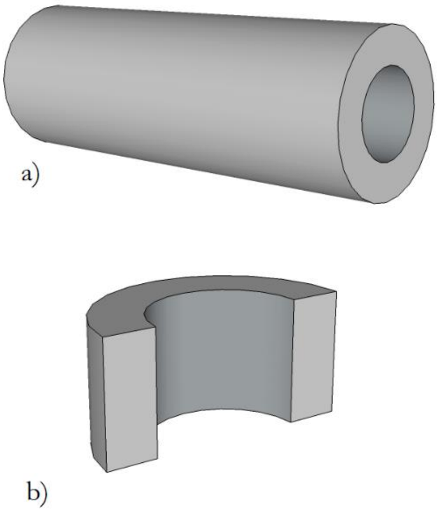

Figure 5.1: steel tube, originally 12 m long, of which a small section is cut (a) and from this, a longitudinal cut allows access to the inner surface (b).

Some classical approaches to surface roughness measurement are:

- Direct image of the surface: combining direct imaging capture and some fast processing, a roughness analysis system can be devised. Although not totally discarded, some aspect suggest that this is not the most promising method for a fast and automated inspection.

- Measurement of scattered intensity: Total Integrated Scattering (TIS) [20], as defined in section 2.3, is a well-known method for roughness measurement, being even implemented for official standards. However, the conditions for its measurement are very demanding and not realistic for our samples. But based in the same idea, we have measured the scattered light by the surface at several angles and points of the sample, trying to check the sensitivity of the method.

- Analysis of speckle: speckle contras is known to be related with the roughness[10,11]. However, this works for small *rms* values, for which speckle is not completely developed, and this is not the case for our samples.

Finally we have proposed a fourth method, based on the illumination of the samples by small spots, smaller than the correlation length of the roughness and study of the spatial distribution of the brightness produced by the local reflectance of the beam on the surface. Strong local slopes should produce large shifts that should be easy to monitor.

5.2 Measurement of scattered light

We are interested in distinguishing a smooth tube from a corrugated one and then, if possible, to assess the degree of corrugation. This light scattering test was done on four surfaces of increasing roughness. Sample S0 has a smooth surface (no corrugation has been induced on it and its surface has the machining finish), and sample S3 has the roughest surface, being samples S1 and S2 intermediate stages.

The measurement was done at two scattering angles θ_1 = 15° and θ_2 = 28° (figure 3.5) and at several position of the sample, averaging the results for four heights.

As we can see in figure 5.1, sample S0 can be distinguished from the others ones, since this sample scatters less light.

However, it is harder to tell apart the three rough surface samples, since the values of the intensity are similar for the three of them. In addition, it is recommended to perform the measurements of the intensity avoiding the specular region since in this zone the dispersion is bigger and the dependence on the exact θ is stronger. If we focus on a region away from the specular, the measurements present less dispersion.

This test has been helpful to prove that a non-corrugated surface could be easily identified in a series of corrugated surfaces. Although it allows us to recognize a smooth sample, we need a method with better precision in order to differentiate samples of different degree of corrugation.

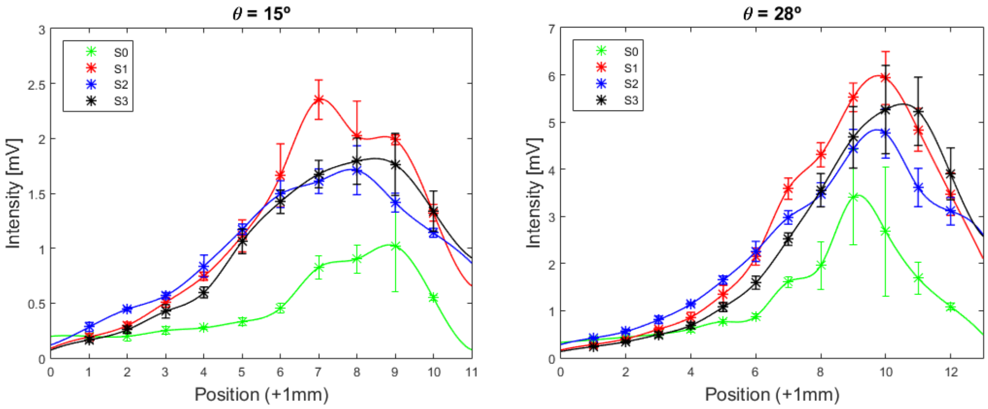

Figure 5.2: intensity of light scattered by 4 samples with surface of different roughness. The intensity has been measured at several points and the error bars indicate the standard deviation. Lines are a guide to the eye.

5.3 Speckle analysis

In general, analysis of the contrast of the speckle pattern is very useful method for our purpose, since surface roughness can be related to the average roughness R_a.

However this method works if the roughness is smaller than the wavelength (less than 0.3 μm working in the visible range) since for a bigger roughness the speckle is completely developed and the contrast saturates.

In the case of our samples, the surface roughness is larger than those values, for the corrugated samples. So, we could again recognize the smooth surface as he only one with $C < 1$. Else, we could go to longer wavelengths, therefore introducing complexity in our experiment.

For this reasons, we have provisionally discarded this method.

5.4 Reflectance of focused beams

The last method we propose is based on the spatial distribution of the maximum of intensity of the scattered light when the size of the illuminating spot is smaller than the typical length of the rough surface.
We suggest that the spatial distribution of this fluctuation could be related to the geometry of the surface profile, more specifically with the local slope of the roughness: the greater the degree of corrugation, the larger the slopes, and correspondingly, the larger the deviation of the scattering with respect to a specular reference.
If we think of this measurement as a dynamic process these variations would mean a fast spatial variation of the "center" of the diffuse scattering.

In order to test this idea, that, to our knowledge, is quiet new in the field, we have measured the surface of some of our samples by means of a 3D coordinate measuring machine equipped with a laser to made non-contact measurements (this equipment was used thanks to the LADICIM lab of the Civil Engineering, UC). From these profiles we can obtain information related to the geometry of the surface, such as the *rms* value, the mean distance to a reference surface $<\Delta y>$, or the mean slope m, that we calculated by doing the derivative of the profile.

Sample / nº of processes	$<\|\Delta y\|>$ **[µm]**	$<m> \pm \sigma_m$	***rms* [µm]**
0	2.1	0.0094 ± 0.0142	2.8
1	4.4	0.0325 ± 0.0462	6.2
Several	14.5	0.099 ± 0.1431	17.5

Table 5.1: mean distance from each point of the profile to a mean surface, mean slope m in each point and RMS for the three samples.

As we can see from table 5.1, both the *rms*, the distance Δy and the mean slope increase with the number of processes of the sample. Another interesting value is $\sigma_m \leq 1.5<m>$, this is implying a broad distribution of the slope values around a mean one.

Now, we would like to relate the values of the slope with the angular distribution of the brighter region of the scattered light since the local reflection establishes that the angle of incidence and reflexion must be the same. Then, for normal incidence, one would expect output beams located around the value 2ϕ (figure 3.7), being $\phi = tan^{-1}(m)$.

From the experimental point of view, the capture of these light distributions is not difficult, but the choice of the best configuration depends on the magnitude of *m*. For small values, the setup described in Chapter 3 (figure 3.6) with an out-of-focus CCD seem ideal. However, for our high values of *m* (severe roughness), the setup described in figure 3.8 seems to be the right one. Then, the surface is illuminated with a laser (λ = 633 nm) and the diffuse reflectance is observed on a screen. The screen is sized 25x13 cm and the images are 3888x2592 pixels.

Figure 5.3: from left to right, original image taken with the camera, image after applying a low pass filer (r = 100 pix.) and image in grey scale: Red points shows the coordinates' origin and green point shows the maximum of the distribution.

As we want to find the maximum of the distribution in a fast way but avoiding spikes (small bright reflections), we decided to smooth the picture by applying a low pass filter (Gaussian filter). The speckle gets blurred, and we then transform the image to 8-bit (grey scale) and find the maximum value. Figure 5.3 shows the process followed to find the maximum of the distribution in all the pictures taken. The red and green points shows the origin and the maximum respectively. This maximum has been plotted in figure 5.4 for the smooth sample (in green), the piece with one corrugation process (in blue) and the piece with several corrugation processes (in black). The red cross shows the point where the laser passes through the screen and the coordinate's origin.

From the experimental results in figure 5.4 we have calculated the mean angle $<2\phi_{exp}>$ at which the maximum appears (represented by the dotted line).
These results can be compared with the ones obtained from the mean slopes *m* of the surface $<2\phi_{m}>$ (represented by the solid line).

All these values are summarized in table 5.2 where it is also shown the mean distance *d* at which the distribution appears on the screen.

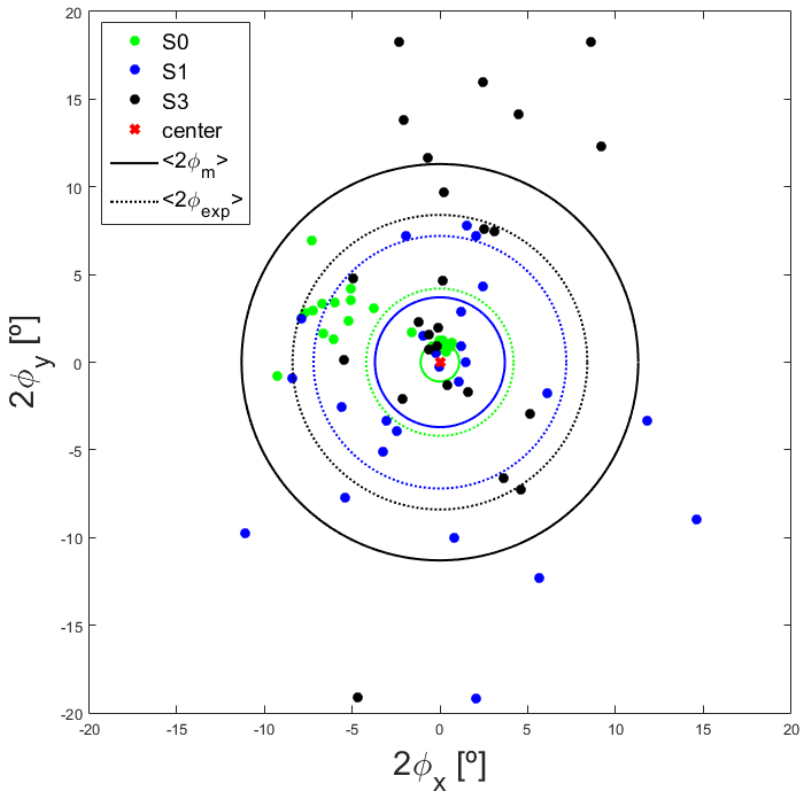

Figure 5.4: spatial distribution of the maximum of intensity for the smooth sample (green), the one with one corrugation process (blue) and the one with several corrugation processes (black). Solid and dotted lines show the 2ϕ values calculated from the mean slopes m and from the experimental pictures. The red cross shows the point where the laser passes through the screen and the coordinate's origin.

Sample / nº of processes	$<m>$	d_m [cm]	$<2\phi_m>$ [º]	d_{exp} [cm]	$<2\phi_{exp}>$ [º]
0	0.0094	0.36	1.1	1.4	4.2
1	0.0325	1.23	3.7	2.4	7.2
Several	0.099	3.80	11.3	2.8	8.4

Table 5.2: mean distance d and mean angle 2ϕ at which the maximum of the distribution appear for the three samples. Subscript m stands for the results obtained from the slope m, and exp for the results obtained from experimental pictures.

Figure 5.4 shows that the greater the degree of corrugation the spreader the distribution of the maximum. We also observe a preference direction of spreading, along the y direction. This may be due to the “fingerprint” caused in the corrugation process. (It is produced by shooting small steel-balls from the inside of the tube while it is rotating. Then, the tangent and radial directions may show a difference in the impact shape). Incidentally, this direction-dependant scattering may be informing of the rotation speed, something that could be useful.

The spatial distribution (angle 2ϕ) obtained from the intensity distribution in the picture are larger than the results obtained from the slopes for the samples S0 and S1. This can be due to imperfection in the surfaces, which, for instance, are very notorious in the smooth piece and enlarge the distribution.

6 CONCLUSIONS AND FUTURE WORK

In this wok we have, first, evaluated the performance of a dynamic imaging spetro-polarimeter adapted to work with samples in the microscopic scale. Secondly, by using an auxiliary setup, we have tested several methods for a fast rough surface characterization based on optics methods.

Concerning the first objective, we have added two different microscope objectives to increase the magnification and then, we have characterized its spatial resolution, that it is consistent with the theoretical one. As a test object, we have used a USAF 1951 test target that is a well-known standard. We get a resolving distance of around 2 μm with the 10x microscope objective so we conclude that we will be able to do microscopic spectro-polarimetry for samples sized in this scale. Table 6.1 summarize the results achieved on this part.

Microscope Objective	***5x***	***10x***
Scale [pix./μm]	2.78	5.74
Experimental resolved distance r *(experimental resolution)*	~3-4 μm (~143 lp/mm)	< 2.2 μm (> 228 lp/mm)
Theoretical/real magnification	5 / 12.90	10 / 26.72

Table 6.1: experimental performance of microscope objectives implemented in the polarimeter.

We have checked the resulting device on a spectrum-sensitive sample sized some tenths of microns, namely, a set of color filter and the liquid crystal layer of a LCD screen of which we have obtain the Mueller matrix at several wavelengths.

We found that the values of the Mueller matrix elements, even when normalized to the intensity values given by element m_{00} are very sensitive to it. We notice the importance of not exceeding the dynamic range of the CCD. In our current conditions it is important to have a homogenous intensity over the field of view, in order to get reliable polarization information.

The next question is: which samples are in the microscopic domain and require our capabilities, i.e. polarimetric and spectral sensibility?
As I already comment in the introduction, our final interest lies in the possibility of imaging the polarization properties of cells.
Of course, there are other improvements in mind, like trying to get a more homogenous intensity in the illuminated region of the sample, maybe by introducing a cylindrical lens after the diaphragm so that we could compensate the spread caused by the grating.

Concerning the second objective, we have reviewed several methods to measure metallic surface roughness and proposed another one that is, to our knowledge, new. We have prepared some experimental setup searching for useful parameters able to connect the scattered intensity with the degree of roughness in a simple and fast way.

We conclude that the light scattering measurement at a single angle is enough to differentiate the smooth sample from the corrugated one, but it is not so useful to assess the degree of roughness. Similar conclusions are obtained for the speckle, mainly because the roughness of these samples in too strong for such technique.

The best results are obtained by studying the spatial distribution of the maximum of the intensity scattered by the surface for a focused beam. We have observed that the fluctuations of this maximum, when the impact point is changed, tends to increase, appearing at larger angles when the roughness of the surface increases. This is due to a broader distribution of the values of the local slopes. We conclude that this method may be the one that provides the right tool for a fast assessment of the different degrees of corrugation.

After this initial test we will like to develop the idea, trying to establish a link between the geometry of the surface and the spatial distribution of the maximum intensity of the scattered light. Eventually, we should be able to assess the degree of roughness in a fast and automatic way within an industrial inspection process.

7 REFERENCES

1. James Hough. *Polarimetry: a powerful diagnostic tool in astronomy.* Astronomy & Geophysics, Vol.47, June 2006.

2. Angelo Pierangelo, Abdelali Benali. *Ex-vivo characterization of human colon cancer by Mueller polarimetric imaging.* Optics Express, Vol. 19, Issue 2, pp. 1582-1593, 2011.

3. H. Arwin, R. Magnusson. *Sum decomposition of Mueller-matrix images and spectra of beetle cuticles.* Optics Express, Vol. 23, Issue 3, pp. 1951-1966, 2015.

4. Michael F. Sterzik, Stefano Bagnulo & Enric Palle. "*Biosignatures as revealed by spectropolarimetry of Earthshine*". Nature, Vol. 483, 64-66, March 2012.

5. Scott Tyo, Dennis L. Goldstein. *Review of passive imaging polarimetry for remote sensing applications.* Applied Optics, Vol. 45, Nº 22, August 2006.

6. Nirmalya Ghosha and I. Alex Vitkin. *Tissue polarimetry: concepts, challenges, applications, and outlook.* Journal of Biomedical Optics 16(11), 110801, November 2011.

7. Maria-Rosaria Antonelli, Angelo Pierangelo. *Mueller matrix imaging of human colon tissue for cancer diagnostics: how Monte Carlo modeling can help in the interpretation of experimental data.* Optics Express, Vol. 18, Issue 10, pp. 10200-10208, 2010.

8. Ceolato R et al. *Light-scattering by aggregates of tumor cells: Spectral, polarimetric, and angular measurements.* Journal of Quantitative Spectroscopy and Radiative Transfer Vol. 146, October 2014.

9. Xuezhen Wang, Jiancheng Lai, and Zhenhua Li. *Polarization studies for backscattering of RBC suspensions based on Mueller matrix decomposition.* Optics Express, Vol. 20, Issue 18, pp. 20771-20782, 2012.

10. Lisa C. Leonard, Vincent Toal. *Roughness measurement of metallic surfaces based on the laser speckle contrast method.* Optics and Lasers in Engineering, Volume 30, Issue 5, pp. 433–440, November 1998.

11. J.B. Meireles et al. *Effect of metallic surface roughness on the speckle pattern formation at diffraction plane*. Optics and Lasers in Engineering, Volume 50, Issue 12, pp. 1731–1734, December 2012.

12. J. M. Sanz Casado. *Polarimetría de sistemas difusores con microestructuras: efectos de difusión múltiple*. Tesis doctoral UC. Julio 2010.

13. C. Extremiana, J. M. Saiz and J. M. Sanz. *Estudio polarimétrico y evalaución de las propiedades ópticas de sistemas sencillos*. Trabajo de fin de Licenciatura en Física. Septiembre 2012. Universidad de Cantabria.

14. F. Carmagnola, J.M Sanz and J.M Saiz. "*Development of a Mueller matrix imaging system for detecting objects embedded in turbid media*". Journal of Quantitative Spectroscopy and Radiative Transfer**,** Volume 146, pp. 199–206, October 2014.

15. A. Fernández, J. M. Saiz, J. M Sanz. *Design and characterization of an imaging spectropolarimeter*. Trabajo Fin de Grado UC. September 2014.

16. J.J. Gil. *Polarimetric characterization of light and media*. Eur. Phys. J. Appl. Phys. 40, 1–47 (2007).

17. Toralf Scharf. *Polarized Liquid Crystals and Polymers*. Chapter 1: polarized light. John Wiley & Sons, 2007. O Bohren chapter 2.

18. Russell A . Chipman. *Handbook of Optics. Chapter 22: Polarimetry*. Mc-Graw Hill, 2009.

19. Shih-Yau Lu and Russell A. Chipman. *Interpretation of Mueller matrices based on polar decomposition*. J. Opt. Soc. Am. A/Vol. 13, No. 5, May 1996

20. Jean M. Bennett. *Introduction to Surface Roughness and Scattering*. Optical Society of America.

21. R.M.A. Azzam. *Photopolarimetric measurement of the Mueller matrix by Fourier analysis of a single detected signal*. Optical Letters, Vol. 2, Nº 6. June 1978.

22. J. Casas. *Óptica, capítulo 38: microscopio*. 6ª edicion. Universidad de Zaragoza, 1985.